Modeling of ac quantum transport through imperfect carbon nanotube interconnects by means of nonequilibrium Green's functions

Emile Vanderstraeten* and Dries Vande Ginste

quest, IDLab, Department of Information Technology, Ghent University/imec, Technologiepark-Zwijnaarde 126, Ghent, Belgium

(Received 25 April 2024; revised 2 September 2024; accepted 6 November 2024; published 2 December 2024)

Because of their long mean free path and superior current-carrying capabilities, carbon nanotubes (CNTs) are considered as an alternative for Cu in future interconnects. To simulate their dynamical properties, a linear equivalent-circuit model is usually invoked containing, among other things, a kinetic inductance and a quantum capacitance. As this equivalent circuit has been derived for perfect CNTs, the effect of imperfections is lacking. Still, imperfections considerably change the CNTs' characteristics, necessitating the development of novel accurate simulation techniques to aid the electronic interconnect designer. Therefore, in this paper, an ac nonequilibrium Green's function modeling technique is constructed for CNT interconnects, yielding a fully quantum mechanical first-principles method. The implemented method abandons the often-used small-signal requirement and includes the self-consistent solution with the Poisson equation. Additionally, a new, generally valid approach to partition a CNT into small units is presented. This allows us to rewrite the Hamiltonian into a block tridiagonal form with small submatrices and, subsequently, to employ the recursive Green's function algorithm in an efficient way. Comparison with the equivalent-circuit model serves as validation of the constructed technique, which is an essential, but challenging, task for periodically driven quantum transport problems. The results show that, in order to accurately model the kinetic inductance, the self-consistent solution with the Poisson equation is a fundamental requirement. The constructed method is used to investigate finite-size effects and vacancies, from which it is argued that local defects can, in the linear equivalent-circuit model, be approximated by means of an additional series resistance as long as the applied bias is small. For a large bias, however, nonlinear effects come into play and the circuit model is no longer valid. Lastly, it is demonstrated, both analytically and numerically, that the even harmonics of the current and the potential are absent within the nearest-neighbor tight-binding approximation for the Hamiltonian of the CNTs.

DOI: 10.1103/PhysRevApplied.22.064005

I. INTRODUCTION

Since the late 1990s, Cu has been the main material of choice for interconnects in integrated circuits. However, its leading position is getting undermined by the continuous downscaling of the critical dimensions of interconnects (and transistors) to meet the unceasing demand for more computational power. The shrinking cross-section dimensions of Cu interconnects aggravate the effect of surface scattering, thereby increasing their resistance and thus degrading their performance in terms of delay times and power dissipation [1]. Moreover, electromigration issues are intensified, affecting the reliability of interconnects [2,3]. A possible alternative to replace Cu in future interconnects are carbon nanotubes (CNTs). These materials of great potential are characterized by a long mean free path and high current-carrying capabilities, thereby mitigating the aforementioned issues of Cu interconnects [3–5].

To analyze the dynamical properties of these CNT interconnects and to integrate them into an electronic design flow, a transmission-line (TL) model, i.e., a linear equivalent-circuit model with distributed components, is usually invoked. Besides the standard transmission-line parameters, i.e., the per-unit-length (PUL) resistance, magnetic inductance, and electrostatic capacitance, additionally a PUL kinetic inductance and quantum capacitance are present. While this TL model was originally derived by means of Luttinger liquid theory [6,7], other similar approaches have been presented as well based on the Boltzmann transport equation [8], a fluid model [9,10], and electron waveguides [11]. This TL model for *perfect* CNTs has been employed as the starting point for ensuing time-domain, variability, and signal-integrity studies of single-walled CNTs and more intricate structures, such as multiwalled CNTs and bundles of CNTs [12–18]. Despite its widespread use, a fundamental understanding

*Contact author: emile.vanderstraeten@ugent.be

 © 2024 American Physical Society

of the implications of imperfections, such as vacancies, Stone-Wales defects, substitutional impurities, strain, and contacts, on the validity of this equivalent-circuit model is lacking. Moreover, as this model consists of linear equations, nonlinear effects have not been considered at all.

To fill this knowledge gap, one can turn to first-principles quantum transport techniques, such as the widely adopted nonequilibrium Green's function (NEGF) formalism [19–23]. In the steady-state case, research into this technique has evolved into a rather mature domain, with several developed simulation codes [24–26]. The effect of strain and several types of defects has already been a topic of study [27–31]. Nevertheless, a steady-state approach is insufficient to fully understand the effect that imperfections have on the CNTs' TL model. Therefore, NEGF techniques specifically adapted to periodically varying biases need to be considered.

A first approach was presented in Ref. [32]. In that paper, starting from the small-signal assumption, an expression was obtained for the current, which varies linearly with the applied bias and subsequently allows for the calculation of the dynamic conductance. In Ref. [33], however, it is argued that this approach leads to nonphysical results, as current conservation and gauge invariance are not satisfied. By a simple partitioning of the displacement current, these fundamental requirements can be satisfied. As a consequence, this current partitioning has been employed by several groups to study the dynamical properties of CNTs [34–38]. Alternatively, the fundamental requirements, i.e., current conservation and gauge invariance, are also satisfied when including Coulomb interaction at the Hartree level, i.e., by solving the NEGF equations self-consistently with the Poisson equation [39,40]. In the case of a CNT field-effect transistor, it has been demonstrated that the two approaches lead to significantly different results [41,42]. Instead of the Poisson equation, the small-signal equations have also been combined with Maxwell's equations to study a CNT-based device [43, 44] and to model the radiation pattern of a quantum-confined quarter-wave monopole antenna [45]. Furthermore, the theoretical foundations have been laid for an ac NEGF method without the small-signal requirement in Refs. [46–48], which allows for the study of nonlinear effects. This method has, for example, been employed to study Floquet topological insulators [49,50], quantum pumps [46,51], and photon-assisted tunneling in quantum-well devices [52].

In this paper, we construct a numerical method with capabilities beyond those of the linear equivalent-circuit model such that imperfect CNTs can be studied too. Therefore, we formulate and implement a novel ac NEGF simulation technique for CNT interconnects embedded in a perfectly electric conducting (PEC) cylinder. The small-signal approximation is abandoned, allowing us to investigate nonlinear behavior. Additionally, to enable the efficient use of the recursive Green's function (RGF) algorithm, a new partitioning procedure that for *all* CNTs results in a small recurring unit is introduced. Furthermore, gauge invariance is satisfied by solving the ac NEGF equations self-consistently with the Poisson equation. The constructed technique is validated by comparing the results to the equivalent-circuit model, which is a crucial, albeit nontrivial, step due to the scarcity of analytical solutions for quantum transport problems under periodically varying biases. Moreover, it allows us to assess the importance of the self-consistent solution with the Poison equation and to identify inaccuracies that are inherently present in techniques based on current partitioning. Lastly, vacancies, edge effects, and nonlinearities are investigated, demonstrating that the presented simulation technique enables us to go beyond the limited capabilities of the linear equivalent-circuit model.

The outline of this paper is as follows. First, the numerical framework is detailed in Sec. II, containing a discussion about the ac NEGF equations and the self-consistent solution with the Poisson equation. Additionally, a method to partition the CNT and subsequently cast the Hamiltonian into a block tridiagonal form is presented. Next, the equivalent-circuit model for the CNT interconnect is briefly described in Sec. III. To validate the constructed method, a comparison with the equivalent-circuit model is made in Sec. IV. Finally, nonlinear behavior, finite-size effects, and vacancies are examined by means of the novel advocated technique, clearly showing its need and appositeness in future interconnect design.

II. NUMERICAL FRAMEWORK

The system under study is a metallic single-walled CNT connected to two metallic electrodes. Within the NEGF framework, this situation is approximated by a finite-length CNT, the central region, that at both ends is connected to a semi-infinite lead. We choose these leads to be CNTs of the same type, which is a valid approximation when the modes of the CNT and the metallic electrodes match well. The central region is enclosed by a metallic cylinder, which is modeled in this paper by a PEC. This PEC serves as the reference conductor, as required in TL modeling [6]. We remark that we have opted for a PEC cylinder (instead of a PEC plane as in Ref. [6]) as it allows us to exploit the rotational symmetry of the setup to simplify the Poisson problem, similarly as in Ref. [41,53]. A zero potential is enforced at the PEC and at the right lead, while a periodically varying bias is applied to the left contact. An illustration of the setup is found in Fig. 1.

The CNT is described by a tight-binding model involving one π electron per atom. The Hamiltonian is of the

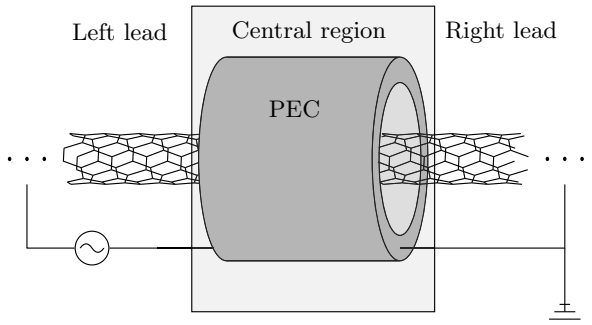

FIG. 1. Setup of the problem. The central region consists of a finite-length CNT that is surrounded by a PEC. The right and left leads are two semi-infinite CNTs that are of the same type. The right lead is connected to the PEC and the ground, while an ac bias is applied to the left lead.

form

$$H = -V_{pp\pi} \sum_{\langle i,j \rangle} a_i^\dagger a_j + \text{H.c.}, \tag{1}$$

with $a_i^\dagger$ and a_j the creation and annihilation operators, respectively. The summation in Eq. (1) is restricted to nearest neighbors only. Note that this model does not include any curvature effects, such as rehybridization of the σ and π states. Therefore, in this paper, only CNTs with diameter larger than 1 nm are considered, for which these hybridization effects are unimportant [54]. The hopping parameter $V_{pp\pi}$ equals -2.75 eV and is the same for all neighbors. When considering the effect of a vacancy on the dynamical properties of CNTs, one lattice point is simply removed from Eq. (1).

A. Ac NEGF

We start the discussion of the NEGF framework with the following time-dependent equations for the retarded and advanced Green's functions, $G^r(t,t')$ and $G^a(t,t')$, respectively, and the lesser Green's function $G^<(t,t')$ [23,32]:

$$\left[i\hbar \frac{\partial}{\partial t} - H(t) \right] G^{r/a}(t,t') - \int dt_1 \, \Sigma^{r/a}(t,t_1) \, G^{r/a}(t_1,t') = I \, \delta(t-t') \tag{2}$$

$$G^<(t,t') = \int dt_1 \int dt_2 \, G^r(t,t_1) \, G^<(t_1,t_2) \, G^a(t_2,t'), \tag{3}$$

with $H(t)$ the Hamiltonian of the central region of the device, and $\Sigma^{r/a}(t,t')$ and $\Sigma^<(t,t')$ the retarded/advanced and lesser self-energy. (Note that superscript $^{r/a}$ is used to avoid the need to duplicate similar retarded and advanced equations.)

In this paper, the discussion is restricted to contact self-energies, which take into account the effect of the semi-infinite leads. Interactions with other particles, such as phonons, are not considered here. The total self-energy sums up the contributions of the different contacts. When referring to the self-energy of a single contact, the subscript α is added to Σ. Both Eqs. (2) and (3) have been expressed in a real-space basis and hence the Hamiltonian H, the Green's functions G, and the self-energies Σ represent matrices. Knowledge of these Green's functions allows for the calculation of several interesting observables, such as current and electron occupation number (see Sec. II B).

To derive the ac NEGF equations, the approach of Ref. [32] is followed and Eqs. (2) and (3) are transformed to the double-energy domain, yielding

$$E \, G^{r/a}(E,E') - \int \frac{dE_1}{2\pi\hbar} H(E_1) \, G^{r/a}(E-E_1,E') = 2\pi\hbar I \, \delta(E-E') + \int \frac{dE_1}{2\pi\hbar} \Sigma^{r/a}(E,E_1) \, G^{r/a}(E_1,E') \tag{4}$$

$$G^<(E,E') = \int \frac{dE_1}{2\pi\hbar} \int \frac{dE_2}{2\pi\hbar} G^r(E,E_1) \Sigma^<(E_1,E_2) \, G^a(E_2,E'). \tag{5}$$

To arrive at these equations, the following conventions for the Fourier transforms were adopted:

$$F(E) = \int_{-\infty}^{+\infty} dt f(t) e^{iEt/\hbar}, \tag{6}$$

$$f(t) = \int_{-\infty}^{+\infty} \frac{dE}{2\pi\hbar} F(E) e^{-iEt/\hbar}, \tag{7}$$

and

$$F(E,E') = \int_{-\infty}^{+\infty} dt \int_{-\infty}^{+\infty} dt' f(t,t') e^{i(Et-E't')/\hbar}, \tag{8}$$

$$f(t,t') = \int_{-\infty}^{+\infty} \frac{dE}{2\pi\hbar} \int_{-\infty}^{+\infty} \frac{dE'}{2\pi\hbar} F(E,E') e^{-i(Et-E't')/\hbar}. \tag{9}$$

If only a constant bias is applied to the contacts, then the system is in the steady-state regime. In this case, the time-dependent Green's functions $G(t,t')$ depend only on the difference $t-t'$ (likewise for the self-energies). In the energy domain, this translates into the property that E must

equal E' and thus, in this steady-state scenario, the Green's functions and self-energies are purely diagonal in energy:

$$G^{\gamma}(E,E') = G^{\gamma}(E)2\pi\hbar\,\delta(E'-E), \tag{10}$$

$$\Sigma^{\gamma}(E,E') = \Sigma^{\gamma}(E)2\pi\hbar\,\delta(E'-E), \tag{11}$$

where γ denotes r, a, or $<$. Substituting Eqs. (10) and (11), and $H(E) = H_0\,2\pi\hbar\,\delta(E) + U_0\,2\pi\hbar\,\delta(E)$, with U_0 the steady-state potential energy, into Eqs. (4) and (5) yields

$$[E \pm i\eta - H_0 - U_0 - \Sigma^{r/a}(E)]\,G^{r/a}(E) = I, \tag{12}$$

$$G^{<}(E) = G^{r}(E)\,\Sigma^{<}(E)\,G^{a}(E), \tag{13}$$

which are the steady-state NEGF equations for the retarded, advanced, and lesser Green's functions.

Furthermore, the lesser contact self-energy is given by

$$\Sigma^{<}(E) = \sum_{\alpha} i\,\Gamma_{\alpha}(E) f_{\alpha}(E), \tag{14}$$

with $\Gamma_{\alpha}(E) = i(\Sigma^{r}_{\alpha}(E) - \Sigma^{a}_{\alpha}(E))$ and $f_{\alpha}(E)$ the Fermi-Dirac function related to contact α. The retarded and advanced self-energies $\Sigma^{r/a}_{\alpha}$ can be found by means of the decimation method of Ref. [55] or by using complex absorbing potentials [56]. Furthermore, in the steady-state regime, the retarded and advanced Green's functions of the considered system are related by means of $G^{r}(E) = (G^{a}(E))^{\dagger}$, with $(G^{a}(E))^{\dagger}$ the Hermitian conjugate of $G^{a}(E)$. A similar relation holds for the retarded and advanced contact self-energies.

In this paper, however, we are interested in the situation where an ac bias is applied to one of the contacts. It is known that the introduction of a sinusoidal signal of frequency ω leads to a correlation between the energies E and $E + n\hbar\omega$ [57], with n an integer value. Consequently, for a bias equal to $-eV_{\mathrm{ac}}\cos(\omega t)$ the contact self-energies develop off-diagonal energy elements and are now given by [32]

$$\Sigma^{\gamma}_{\alpha}(E,E') = \sum_{n} \mathcal{S}^{\gamma}_{\alpha,0,n}(E)\,2\pi\hbar\,\delta(E-E'+n\hbar\omega), \tag{15}$$

with

$$\mathcal{S}^{\gamma}_{\alpha,m,n}(E) = \sum_{l}(-1)^{n-m}J_{n-m+l}\left(\frac{eV_{\mathrm{ac},\alpha}}{\hbar\omega}\right) \times J_{l}\left(\frac{eV_{\mathrm{ac},\alpha}}{\hbar\omega}\right)\Sigma^{\gamma}_{\alpha}(E+m\hbar\omega-l\hbar\omega). \tag{16}$$

The function J_l is a Bessel function of the first kind and order l. The summation running over l includes all integer values. It is readily shown that $\mathcal{S}^{\gamma}_{\alpha,0,n}$ obeys the property

$$\mathcal{S}^{\gamma}_{\alpha,0,n}(E) = \mathcal{S}^{\gamma}_{\alpha,m,n+m}(E-m\hbar\omega). \tag{17}$$

Equation (15) indicates that off-diagonal elements are only possible when the difference between the energies $E - E'$ is an integer times $\hbar\omega$, with ω the angular frequency of the applied bias. If we consider the following series expansion for the Bessel function of the first kind,

$$J_l(z) = \left(\frac{z}{2}\right)^{l}\sum_{k=0}^{+\infty}(-1)^{k}\frac{(z^2/4)^{k}}{k!\,\Gamma(l+k+1)}, \tag{18}$$

with $\Gamma(z)$ the Gamma function, it is evident that $\mathcal{S}^{\gamma}_{\alpha,0,n}$ scales with $V_{\mathrm{ac},\alpha}$ to the power n or more. Consequently, when the applied bias $V_{\mathrm{ac},\alpha}$ equals zero, all off-diagonal terms are zero too and Eq. (15) reduces indeed to the steady-state situation in Eq. (11). In the small-bias regime, additionally, the $n = 1$ off-diagonal terms are involved in the calculations. The larger the bias $V_{\mathrm{ac},\alpha}$, compared to $\hbar\omega/e$, the more off-diagonal terms need to be considered. Note that, to numerically evaluate Eq. (16), only Σ^{γ}_{α}, the steady-state self-energy, is required at different energies.

To account for Coulomb effects at the Hartree level, each harmonic of the potential energy $U(t) = -e\,\phi(t)$, with ϕ the scalar potential, is related to the corresponding harmonic of the electron density by means of the Poisson equation. At the same time, the electron occupation number and thus also the electron density are obtained by solving the ac NEGF equations (see Sec. II B). Consequently, solving these equations self-consistently implies that the Hamiltonian periodically depends on time:

$$H(t) = H_0 + U(t) = H_0 + \sum_{n=-\infty}^{+\infty} U_n e^{in\omega t}, \tag{19}$$

where U_n are complex diagonal matrices, satisfying the additional condition that $U_n = U^{\dagger}_{-n}$, as $U(t)$ should be real-valued. To account for nonlinear behavior, originating from the ac NEGF equations, higher harmonics $n\omega$ are included in addition to the fundamental frequency ω. Transforming Eq. (19) to the energy domain by means of Eq. (6) results in

$$H(E) = H_0\,2\pi\hbar\,\delta(E) + \sum_{n=-\infty}^{+\infty} U_n\,2\pi\hbar\,\delta(E+n\hbar\omega). \tag{20}$$

At this point the small-bias approximation is often invoked to circumvent the, at first sight, cumbersome expressions in Eqs. (4) and (5) [32,41]. Only the terms linear in the bias amplitude $-eV_{\mathrm{ac}}$ are retained, simplifying the equations considerably. As a drawback, nonlinearities cannot be analyzed with such a technique. Hence, in this paper,

this approximation is abandoned and the full ac NEGF equations are considered.

When substituting Eqs. (15) and (20) into Eqs. (4) and (5), it follows that the Green's functions are zero when the difference $E - E'$ does not equal an integer times $\hbar\omega$. Therefore, a similar expression as for the self-energy is valid:

$$G^{\gamma}(E,E') = \sum_{n} \mathcal{G}^{\gamma}_{0,n}(E) 2\pi\hbar\,\delta(E - E' + n\hbar\omega). \tag{21}$$

Additionally, we define

$$\mathcal{G}^{\gamma}_{0,n}(E) = \mathcal{G}^{\gamma}_{m,n+m}(E - m\hbar\omega). \tag{22}$$

Finally, Eqs. (4) and (5) reduce to

$$(E + m\hbar\omega - H_0)\mathcal{G}^{r/a}_{m,n}(E) - \sum_{n_1}[U_{n_1-m} + \mathcal{S}^{r/a}_{m,n_1}(E)]\mathcal{G}^{r/a}_{n_1,n}(E) = \delta_{m,n} \tag{23}$$

and

$$\mathcal{G}^{<}_{m,n}(E) = \sum_{n_1,n_2} \mathcal{G}^{r}_{m,n_1}(E)\mathcal{S}^{<}_{n_1,n_2}(E)\mathcal{G}^{a}_{n_2,n}(E). \tag{24}$$

The integrals over the energy have now been replaced by summations over integers.

Equations (23) and (24) are rewritten as

$$(EI - \mathcal{H} - \mathcal{S}^{r/a}(E) - \mathcal{U})\mathcal{G}^{r/a}(E) = I \tag{25}$$

and

$$\mathcal{G}^{<}(E) = \mathcal{G}^{r}(E)\mathcal{S}^{<}(E)\mathcal{G}^{a}(E), \tag{26}$$

with

$$\mathcal{H} = \begin{pmatrix} \ddots & \vdots & \vdots & \vdots & \iddots \\ \cdots & H_0 + \hbar\omega & 0 & 0 & \cdots \\ \cdots & 0 & H_0 & 0 & \cdots \\ \cdots & 0 & 0 & H_0 - \hbar\omega & \cdots \\ \iddots & \vdots & \vdots & \vdots & \ddots \end{pmatrix}, \tag{27}$$

$$\mathcal{S}^{\gamma} = \begin{pmatrix} \ddots & \vdots & \vdots & \vdots & \iddots \\ \cdots & \mathcal{S}^{\gamma}_{-1,-1} & \mathcal{S}^{\gamma}_{-1,0} & \mathcal{S}^{\gamma}_{-1,1} & \cdots \\ \cdots & \mathcal{S}^{\gamma}_{0,-1} & \mathcal{S}^{\gamma}_{0,0} & \mathcal{S}^{\gamma}_{0,1} & \cdots \\ \cdots & \mathcal{S}^{\gamma}_{1,-1} & \mathcal{S}^{\gamma}_{1,0} & \mathcal{S}^{\gamma}_{1,1} & \cdots \\ \iddots & \vdots & \vdots & \vdots & \ddots \end{pmatrix}, \tag{28}$$

$$\mathcal{G}^{\gamma} = \begin{pmatrix} \ddots & \vdots & \vdots & \vdots & \iddots \\ \cdots & \mathcal{G}^{\gamma}_{-1,-1} & \mathcal{G}^{\gamma}_{-1,0} & \mathcal{G}^{\gamma}_{-1,1} & \cdots \\ \cdots & \mathcal{G}^{\gamma}_{0,-1} & \mathcal{G}^{\gamma}_{0,0} & \mathcal{G}^{\gamma}_{0,1} & \cdots \\ \cdots & \mathcal{G}^{\gamma}_{1,-1} & \mathcal{G}^{\gamma}_{1,0} & \mathcal{G}^{\gamma}_{1,1} & \cdots \\ \iddots & \vdots & \vdots & \vdots & \ddots \end{pmatrix}, \tag{29}$$

$$\mathcal{U} = \begin{pmatrix} \ddots & \vdots & \vdots & \vdots & \iddots \\ \cdots & U_0 & U_1 & U_2 & \cdots \\ \cdots & U_{-1} & U_0 & U_1 & \cdots \\ \cdots & U_{-2} & U_{-1} & U_0 & \cdots \\ \iddots & \vdots & \vdots & \vdots & \ddots \end{pmatrix}. \tag{30}$$

As a result, the ac NEGF equations for the retarded, advanced, and lesser Green's functions in Eqs. (25) and (26) have the exact same form as the steady-state Eqs. (12) and (13). In the ac NEGF case, however, the equations have been formulated in an enlarged space $\mathcal{R} \otimes \mathcal{T}$, also called the Floquet-Sambe space, where $\mathcal{R}$ represents the real space and $\mathcal{T}$ the space spanned by the basis functions $e^{-in\omega t}$ [48,50].

As the matrices in Eqs. (27)–(30) are of infinite size, a cutoff $h_{\max}$ is introduced to enable numerical computations. In this way, n ranges between $-h_{\max}$ and $h_{\max}$. Thus, $2h_{\max} + 1$ basis functions are retained in the space $\mathcal{T}$. As already argued above, increasing the amplitude V_{ac} of the applied bias at the contacts increases the size of the off-diagonal terms in Eq. (28). Hence, for increasing V_{ac}, more off-diagonal terms need to be taken into account, i.e., a larger $h_{\max}$ is required, in order to obtain accurate results. This will be demonstrated further in Sec. IV E.

B. Observables

Starting from the Green's functions, expressions for the observables, number of electrons, and current are derived. In the time domain, they have the following form [23,32]:

$$I_{\alpha}(t) = 2e \int dt_1\, \mathrm{Tr}[G^{r}(t,t_1)\Sigma^{<}_{\alpha}(t_1,t) + G^{<}(t,t_1)\Sigma^{a}_{\alpha}(t_1,t) - \Sigma^{r}_{\alpha}(t,t_1)G^{<}(t_1,t) - \Sigma^{<}_{\alpha}(t,t_1)G^{a}(t_1,t)], \tag{31}$$

$$N(t) = -2i\hbar\,\mathrm{Diag}[G^{<}(t,t)]. \tag{32}$$

Note that a factor 2 was immediately added to both the number of electrons (per lattice site) $N(t)$ and the current $I_{\alpha}(t)$. Since the Hamiltonian does not contain spin-dependent terms, this extra degree of freedom still needs to be corrected for in the expressions for the observables.

By transforming Eqs. (31) and (32) to the energy domain and by casting them into the forms $N(E) = \sum_n N_n 2\pi\hbar\,\delta(E + n\hbar\omega)$ and $I_\alpha(E) = \sum_n I_{\alpha,n} 2\pi\hbar\,\delta(E + n\hbar\omega)$, one obtains

$$I_{\alpha,n} = 2e\int_{-\infty}^{+\infty}\frac{dE}{2\pi\hbar}\,\mathrm{Tr}\{[\mathcal{G}^<(E)\mathcal{S}^a_\alpha(E) + \mathcal{G}^r(E)\mathcal{S}^<_\alpha(E) - \mathcal{S}^<_\alpha(E)\mathcal{G}^a(E) - \mathcal{S}^r_\alpha(E)\mathcal{G}^<(E)]_{0,n}\}, \tag{33}$$

$$N_n = -2i\hbar\int_{-\infty}^{+\infty}\frac{dE}{2\pi\hbar}\,\mathrm{Diag}[\mathcal{G}^<_{0,n}]. \tag{34}$$

When setting $n = 0$ and replacing $\mathcal{G}$ and $\mathcal{S}$ by G and Σ, respectively, again the same equations as in steady state are obtained [23]. Compared to the steady-state case, after introducing the cutoff parameter $h_{\max}$, the size of the basis is extended by a factor $2h_{\max} + 1$. Hence, calculating every element of the inverse in Eq. (25) quickly becomes intractable, as this operation scales cubically with the size of the matrix. Because Eqs. (33) and (34) only involve parts of this inverse due to the local nature of the contact self-energies, the recursive Green's function algorithm [58,59] is a considerable improvement over direct inversion for quasi-one-dimensional systems. However, it requires the matrix to be block tridiagonal. We remark that by changing the order of the basis functions, the matrix $(EI - \mathcal{H} - \mathcal{S}^{r/a}(E) - \mathcal{U})$ can be brought into this form under the condition that the Hamiltonian H_0 is also block tridiagonal. Therefore, our attention must shift from $(EI - \mathcal{H} - \mathcal{S}^{r/a}(E) - \mathcal{U})$ to H_0.

C. Partitioning of the Hamiltonian

Partitioning CNTs into small recurring building blocks or unit cells of which the lattice sites interact only with other lattice sites of the same or neighboring building blocks naturally leads to a Hamiltonian that is block tridiagonal. Consequently, the RGF algorithm can be invoked to determine the relevant parts of the retarded Green's function. This has been demonstrated for zigzag and armchair CNTs in Ref. [53]. The size of the fundamental unit cell is quite crucial, as the RGF algorithm scales cubically with it. For chiral CNTs, however, this size can become very large following the traditional approach of Ref. [54,60,61]. For a general (n, m) CNT, the number of carbon atoms inside such a unit cell amounts to [54,60,61]:

$$\frac{4(n^2 + nm + m^2)}{\tau\,\gcd(n, m)}, \tag{35}$$

with $\gcd(n, m)$ the greatest common divisor of n and m, and where $\tau = 3$ if $(n - m)/3\,\gcd(n, m)$ is integer and $\tau = 1$ otherwise. When a greatest common divisor can be found, the number of carbon atoms in a unit cell reduces significantly. For armchair and zigzag CNTs, for example, expression (35) results in $4n$. For chiral nanotubes, this is not necessarily the case, and the number of carbon atoms in a unit cell may become very large; e.g., for a $(16, 13)$ CNT, expression (35) equals 844.

To enable efficient calculations for *all* types of CNTs by means of the RGF algorithm, we introduce a new type of partitioning. Therefore, the fundamental building block or unit cell of the CNT should meet three requirements:

(a) The unit cells are identical and matrices describing the interactions between the unit cells should be the same along the entire length of the nanotube.

(b) Unit cells interact only with neighboring ones. In this way, the Hamiltonian reduces to a block tridiagonal form.

(c) The unit cells should be small, as the RGF algorithm scales cubically with the number of lattice points inside one unit cell.

To construct such a unit cell, we start from a graphene layer, as depicted in Fig. 2. The lattice vectors of graphene are defined by $\mathbf{u} = (1, 0)$ and $\mathbf{v} = (1/2, \sqrt{3}/2)$, which are normalized to 1 to simplify the discussion. The lattice of graphene is invariant under translations defined by $i\mathbf{u} + j\,\mathbf{v}$, with i and j integers. For an (n, m) CNT the circumference is described by $\mathbf{c} = n\mathbf{u} + m\mathbf{v}$. All lattice points that are an integer times $\mathbf{c}$ distanced from each other are, because of the periodic boundary conditions, the same points on a CNT. As one side of the unit cell, we take the vector $\mathbf{c}$. In this way, the interface between two unit cells is perpendicular to the axis of the tube. The unit cells are required to be the same along the entire length of the CNT. When the other side of the unit cell is $i\mathbf{u} + j\,\mathbf{v}$, with i and j integer, this condition is satisfied. To simplify the discussion, only $\mathbf{u}$ and $\mathbf{v}$ are considered. If $n \geq m$ we opt for $\mathbf{v}$, while $\mathbf{u}$ is chosen for the case $m \geq n$. The $n = m$ case is a limiting situation for which both $\mathbf{u}$ and $\mathbf{v}$ can be employed to construct the unit cell. In Fig. 2, such a unit cell is constructed for a $(5, 3)$ CNT (gray region). If $\mathbf{u}$ had been chosen instead of $\mathbf{v}$, which is depicted by the hatched region in Fig. 2, the hopping interaction between lattice points A and B would be an interaction between two next-nearest-neighbor unit cells, violating the second requirement.

Now we prove that, with the above choices for the sides of the unit cell, there are only interactions between neighboring unit cells. Consider the case $n \geq m$. We first introduce the vector $\mathbf{l}$, which is perpendicular to $\mathbf{c}$ and has length ΔL, i.e., the thickness of the unit cell (see Fig. 2). This vector $\mathbf{l}$ is given by

$$\mathbf{l} = \frac{\sqrt{3}n}{2(n^2 + nm + m^2)}\left(-\frac{\sqrt{3}}{2}m, n + \frac{1}{2}m\right), \tag{36}$$

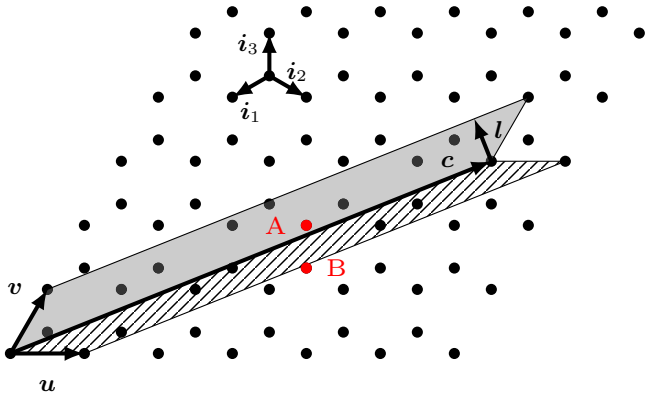

FIG. 2. Schematic of the construction of a unit cell, described by **c** and **v**, of a (5, 3) CNT.

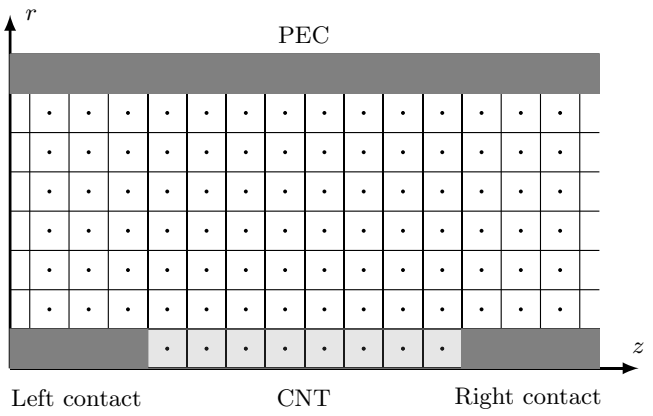

FIG. 3. Schematic of the grid of the Poisson problem.

with

$$\Delta L = \frac{\sqrt{3}n}{2\sqrt{n^2+nm+m^2}}. \tag{37}$$

For the second requirement to be satisfied, the length of the orthogonal projection of the three possible interaction vectors, i.e., $\mathbf{i}_1 = (-1/2, -1/(2\sqrt{3}))$, $\mathbf{i}_2 = (1/2, -1/(2\sqrt{3}))$, and $\mathbf{i}_3 = (0, 1/\sqrt{3})$, onto **l** should be smaller than or equal to ΔL. As n and m are whole numbers, this results in the three inequalities

$$m^2 - 2nm + n^2 \leq 9n^2, \tag{38}$$

$$4m^2 + 4nm + n^2 \leq 9n^2, \tag{39}$$

$$m^2 + 4nm + 4n^2 \leq 9n^2, \tag{40}$$

which are all valid for $n \geq m$, concluding the proof that unit cells only interact with neighboring ones. It is readily shown that the unit cell contains exactly $2n$ lattice points and thus that the block matrices of the Hamiltonian H_0 written into block tridiagonal matrix form are of size $2n \times 2n$. The case $m \geq n$ is completely analogous.

D. Self-consistent solution with the Poisson equation

Coulomb interactions are taken into account up to the Hartree level, which is equivalent to self-consistently solving the NEGF equations with the Poisson equation. Each harmonic of the scalar potential is related to the corresponding harmonic of the electron density by means of the Poisson equation

$$\nabla \cdot \epsilon \nabla \phi_n = -\rho_n, \tag{41}$$

with n the number of the harmonic, ϵ the dielectric permittivity, ϕ_n the scalar potential, and ρ_n the charge density. As the structure under study is rotationally invariant along its axis, the Poisson equation is converted to a cylindrical coordinate system:

$$\frac{1}{r}\frac{\partial}{\partial r}\left(r\epsilon\frac{\phi_n}{\partial r}\right) + \frac{\partial}{\partial z}\epsilon\frac{\partial \phi_n}{\partial z} = -\rho_n. \tag{42}$$

In a next step, the r axis and the z axis are discretized into N_r and N_z grid cells, respectively. The entire grid is depicted in Fig. 3. The left contact, right contact, and PEC, represented by the dark gray regions, have not been gridded, as their potential is uniformly distributed. The unit cells of the CNT, indicated in light gray, are the same as the unit cells defined for the quantum transport problem in Sec. II C. The charge density and the potential are evaluated at the center of each grid cell. Employing central difference approximations, the continuous equation (42) is discretized into

$$A\mathbf{\Phi}_n + \mathbf{\Psi}_{\mathrm{BC},n} = \boldsymbol{\rho}_n, \tag{43}$$

with $\mathbf{\Phi}_n$ and $\boldsymbol{\rho}_n$ vectors containing the values of ϕ_n and ρ_n, respectively, at all grid cells. The matrix A, which is the same for all harmonics, and the vector $\mathbf{\Psi}_{\mathrm{BC},n}$, which includes the effect of the boundary conditions, follow from the discretization procedure.

In our problem setting, the charges depend on the Hamiltonian via Eq. (34) and thus on the potential energy U_n [see Eq. (20)]. This renders the rhs of Eq. (43), $\boldsymbol{\rho}_n$, a function of the scalar potential $\mathbf{\Phi}_n$. Moreover, the different harmonics are also coupled through the NEGF equations. Solving the NEGF equations and Eq. (43) self-consistently in an iterative way is inefficient and often results in convergence issues. Hence, we define

$$\mathbf{F}(\mathbf{\Phi}_{\mathrm{tot}}) = A_{\mathrm{tot}}\mathbf{\Phi}_{\mathrm{tot}} - \boldsymbol{\rho}_{\mathrm{tot}}(\mathbf{\Phi}_{\mathrm{tot}}) + \mathbf{\Psi}_{\mathrm{BC,tot}}, \tag{44}$$

where $\mathbf{\Phi}_{\mathrm{tot}}$ is a concatenation of the vectors $\mathbf{\Phi}_n$ for n ranging from $-h_{\max}$ to $+h_{\max}$. The vectors $\boldsymbol{\rho}_{\mathrm{tot}}$ and $\mathbf{\Psi}_{\mathrm{BC,tot}}$ are

constructed in a similar way, while A_{tot} is a block diagonal matrix consisting of the matrices A.

To determine $\mathbf{\Phi}_{\text{tot}}$ for which $\mathbf{F} = 0$, Broyden's method [62] is invoked. Note, however, that the vector $\mathbf{\Phi}_{\text{tot}}$ has a size of approximately $N_r \times N_z \times (2h_{\max} + 1)$. To ease the calculations required for the nonlinear problem, the functional of Eq. (44), $\mathbf{F}(\mathbf{\Phi}_{\text{tot}})$, is replaced by

$$P_{\text{CNT}}\mathbf{\Phi}_{\text{tot}} - P_{\text{CNT}}A_{\text{tot}}^{-1}[\boldsymbol{\rho}_{\text{tot}}(P_{\text{CNT}}\mathbf{\Phi}_{\text{tot}}) + \mathbf{\Psi}_{\text{BC,tot}}], \quad (45)$$

with P_{CNT} a projection matrix, restricting vectors defined on the entire grid (Fig. 3) only to the light gray cells associated with the CNT. In this way, the problem has been reduced to finding $P_{\text{CNT}}\mathbf{\Phi}_{\text{tot}}$ for which Eq. (45) is equal to zero. This system of equations, in contrast, is of size $N \times (2h_{\max} + 1)$. To connect $P_{\text{CNT}}\mathbf{\Phi}_{\text{n}}$ to U_n of Sec. II A, one needs additionally to multiply by the charge of an electron $-e$. Similarly, the connection between N_n, the number of electrons at a lattice point, and $P_{\text{CNT}}\boldsymbol{\rho}_{\text{n}}$, the charge density, is readily made.

III. EQUIVALENT-CIRCUIT MODEL

In Fig. 4 the equivalent-circuit model of a CNT interconnect is depicted as originally proposed in Refs. [6,7]. At the left and right ends, the model is terminated by a contact resistance R_c that equals $1/(4G_0)$, with G_0 the quantum of conductance $2e^2/h$. The gray region should be understood in a distributed way, as a concatenation of infinitesimally small circuit elements or, equivalently, as a transmission line with per-unit-length inductance, resistance, and capacitance. The electrochemical potential $\mu(z,t)$ and current $I(z,t)$ are then governed by the telegrapher's equations [8,9]

$$C_T\frac{\partial\mu(z,t)}{\partial t} = -\frac{\partial I(z,t)}{\partial z}, \quad (46)$$

$$L_T\frac{\partial I(z,t)}{\partial t} + RI(z,t) = -\frac{\partial\mu(z,t)}{\partial z}, \quad (47)$$

with the total PUL inductance

$$L_T = L_M + \frac{L_K}{4}, \quad (48)$$

the total PUL capacitance

$$C_T = \left(\frac{1}{C_E} + \frac{1}{4C_Q}\right)^{-1}, \quad (49)$$

and the PUL resistance R. Besides the magnetic inductance L_M and the electrostatic capacitance C_E, which are also present in transmission-line models for traditional interconnects, an additional kinetic inductance $L_K = 1/(G_0 v_F)$

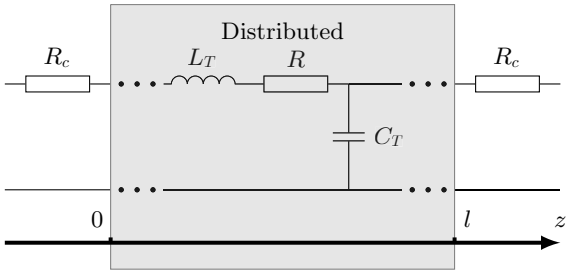

FIG. 4. Equivalent circuit of a CNT enclosed by a cylindrical PEC.

and quantum capacitance $C_Q = G_0/v_F$, with v_F the Fermi velocity, are added to account for the cross-sectional confinement.

The model was originally proposed for a perfect CNT above a PEC plane [6]. In this work, however, we use a PEC cylinder and thus adopt the following values for electrostatic capacitance and magnetic inductance:

$$C_E = \frac{2\pi\epsilon}{\ln(b/a)}, \quad (50)$$

$$L_M = \frac{\mu}{2\pi}\ln(b/a), \quad (51)$$

with a the radius of the CNT and b the radius of the PEC cylinder. As the size of the magnetic inductance is typically several orders of magnitude smaller than the

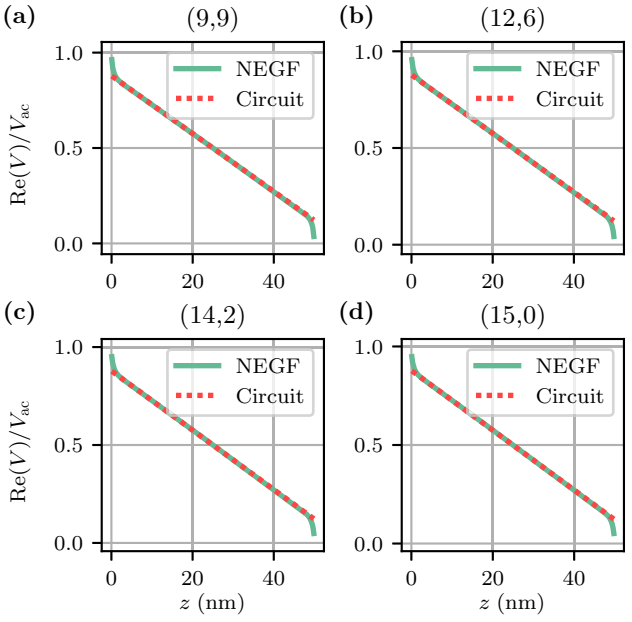

FIG. 5. Real part of the potential V as a function of the position z for four different types of CNTs, calculated by means of both the constructed NEGF technique and the equivalent-circuit model. The PEC cylinder has been left out.

kinetic inductance, it is omitted in the remainder, similarly as in Refs. [6,8]. Additionally, electron-phonon scattering is not taken into account in the modeling technique, and thus, to make a valid comparison, R, the PUL resistance, is put equal to zero. We remark, though, that, within the NEGF framework, scattering with phonons can be included perturbatively, but this is left for future work.

While in Eqs. (46) and (47) the transmission-line model is based on the electrochemical potential $\mu(z,t)$, an equivalent model also exists for the Poisson potential $V(z,t) = U(z,t)/(-e)$ and it is retrieved by exploiting the relation $V(z,t) = \mu(z,t)C_T/C_E$ [8,9].

The situation without PEC will be studied first, as it allows us to verify the constructed method step by step. Without a reference conductor, the model reduces to the series connection of two contact resistances with a kinetic inductance, resulting in the following expression for V in the frequency domain:

$$V(z) = \frac{R_C + j\omega L_T(l-z)}{Z} V_{\text{ac}}, \tag{52}$$

with impedance $Z = 2R_C + j\omega L_T l$. Note that, in contrast to Sec. II, the traditional convention—in the domain of electronics—for time-harmonic signals is used, adopting a $e^{+j\omega t}$ time dependence, with j the imaginary unit. In the general case, with reference conductor, Eqs. (46) and (47) can also be solved analytically, giving rise to a potential profile

$$V(z) = \frac{2R_C\cos(k(l-z)) + 2jZ_0\sin(k(l-z))}{4R_C\cos(kl) + 2j\,(Z_0 + R_C^2/Z_0)\sin(kl)} \frac{C_T}{C_E} V_{\text{ac}}, \tag{53}$$

with wave number $k = \omega\sqrt{L_T C_T}$ and characteristic impedance $Z_0 = \sqrt{L_T/C_T}$. The total impedance of the CNT with reference conductor, which is defined as $Z = V_{\text{ac}}/I(0)$, is given by

$$Z = \frac{4R_C Z_0\cos(kl) + 2j\,(Z_0^2 + R_C^2)\sin(kl)}{2Z_0\cos(kl) + 2jR_C\sin(kl)}. \tag{54}$$

IV. RESULTS

A. Without PEC

To validate the constructed method step by step, the situation without PEC is considered first. This allows one to check whether the constructed technique successfully includes the kinetic inductance. To be able to compare to the equivalent-circuit model, a small bias $V_{\text{ac}} = 0.1$ mV is applied to the left contact such that no nonlinear effects appear. This additionally implies that $h_{\max} = 1$ suffices. All CNTs in this section have a diameter of approximately 1.2 nm and a length of 50 nm. Along the r axis, 200 grid cells are taken for the Poisson problem and a relative permittivity $\epsilon_r = 1$ is considered. The employed frequency f is 10 THz. In addition, room temperature ($T = 298$ K) is used for all simulations.

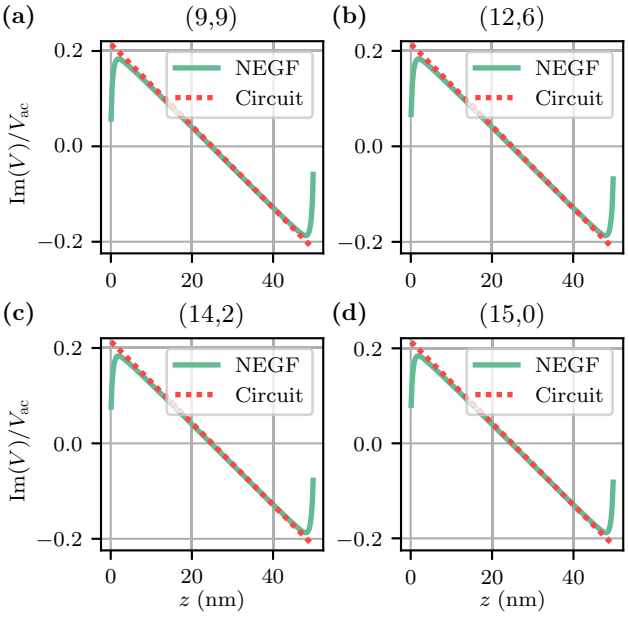

FIG. 6. Imaginary part of the potential V as a function of the position z for four different types of CNTs, calculated by means of both the constructed NEGF technique and the equivalent-circuit model. All CNTs are 50 nm long. The PEC cylinder has been left out.

Figure 5 shows the results for the real part of the potential V, while those for the imaginary part are given in Fig. 6. Note that all three types of metallic CNTs have been considered. CNT $(15,0)$ belongs to the zigzag category, while $(9,9)$ is an armchair CNT. The remaining two CNTs, $(12,6)$ and $(14,2)$, are of the chiral type. Figures 5 and 6 demonstrate that the curves calculated via the constructed NEGF approach, which includes Coulomb effects through the self-consistent solution with the Poisson equation, align perfectly with the equivalent-circuit model for every considered CNT. The slope of the potential, which originates from the presence of the kinetic inductance, is the same for both methods. Only near the ends can one observe a difference between the two approaches. For the equivalent-circuit model, the contact resistances cause a discontinuous jump, while the NEGF curves remain smooth. For CNTs of approximately the same diameter and length, but of different type, the results are very similar. Therefore, subsequent plots only show the results for a single type of CNT.

The conductance $\text{Re}(1/Z)$ and susceptance $\text{Im}(1/Z)$ are studied as a function of the frequency f for the $(15,0)$ zigzag CNT in Fig. 7. Besides the equivalent-circuit model and the constructed method, the results for NEGF in combination with the current partitioning procedure of Ref. [33] are also plotted, as it has been used before

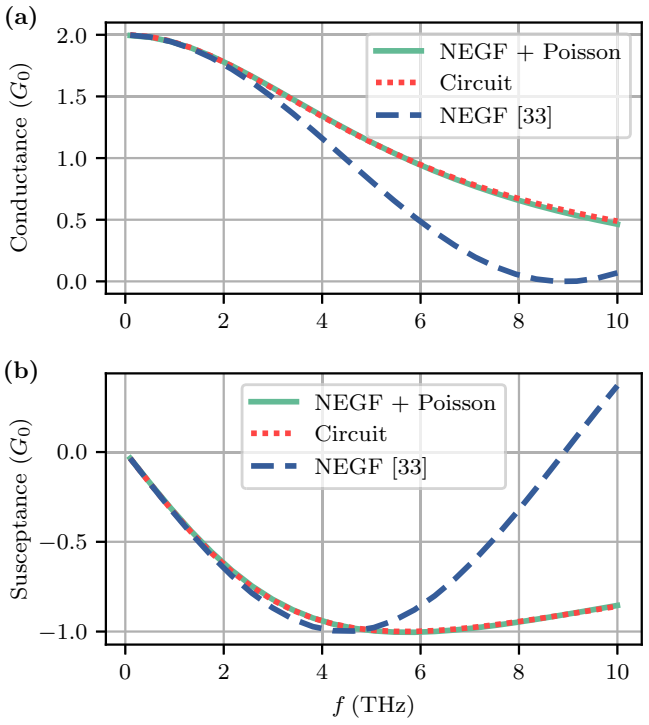

FIG. 7. The (a) conductance and (b) susceptance of a 50-nm long (15, 0) CNT as a function of the frequency f. Three methods are compared: the equivalent-circuit model, NEGF in combination with the partitioning approach of Ref. [33], and NEGF self-consistently solved with the Poisson equation. The PEC cylinder has been left out.

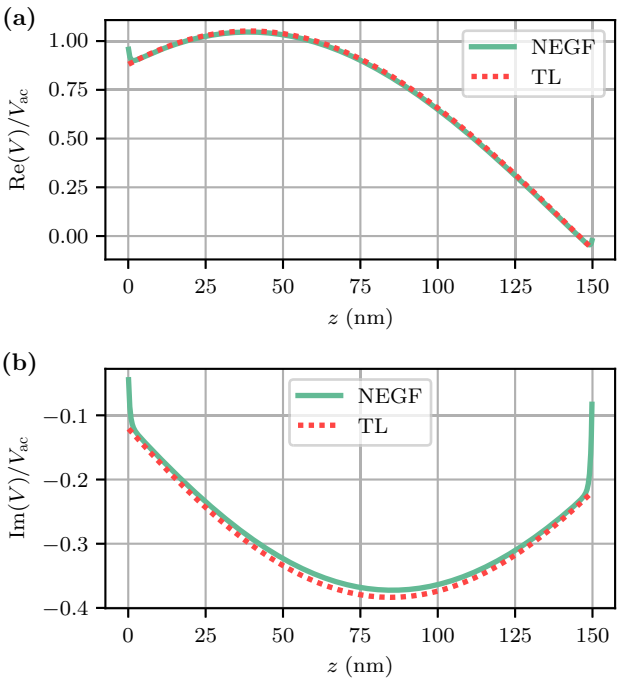

FIG. 8. The (a) real and (b) imaginary parts of the potential V as a function of the position z for a 150-nm long (14, 2) CNT, calculated via the constructed NEGF technique and the equivalent-circuit model. The CNT is enclosed by a PEC cylinder.

to study CNTs [34–38]. All three methods exhibit the expected small-frequency behavior: the susceptance goes to zero, while the conductance approaches twice the quantum of conductance G_0. However, for larger values of the frequency, the method employing current partitioning deviates significantly from the other two.

It appears that the self-consistent solution with the Poisson equation is essential in ac NEGF approaches to accurately include the kinetic inductance. In the considered situation, electrons traversing the device are affected not by a static potential but by an oscillating one. When a particle is injected at the left contact, a certain potential is present in the device. The moment the particle arrives at a particular point along the CNT, however, this potential will have changed already. The longer the device and the shorter the period of the oscillations, the larger the difference will be between the two situations. This explains why the two methods, the current partitioning approach and the self-consistent solution with the Poisson equation, differ considerably for large frequencies, while they converge to each other in the low-frequency limit. In the current partitioning approach, the device region's potential remains constant over time, while the potential correctly fluctuates as a function of time for our advocated method.

B. With PEC

Next, the situation with PEC cylinder is considered. The simulation setup is similar to the one discussed in Sec. IV A, except for the presence of a PEC cylinder, which has a radius 20 times larger than that of the CNT. Additionally, the CNT is now 150-nm long. The results for the potential are presented in Fig. 8. It is again demonstrated that the constructed technique agrees very well with the equivalent-circuit model. For both the imaginary part and the real part, the solid green line, representing the proposed NEGF technique, and the red dashed line, which is related to the TL model, are on top of each other. In contrast to Figs. 5 and 6, wave effects are now observed. Owing to the presence of the PEC cylinder and the related electrostatic and quantum capacitance, the equivalent-circuit model becomes a transmission line, which is modeled by a wave equation for the potential and the current.

Besides the potential, the conductance and the susceptance are also given as a function of the frequency f in Fig. 9. It is evident that the current partitioning approach [33] is inaccurate in this case, as it is unable to include the electrostatic capacitance. In contrast, the results illustrate that the proposed technique, which solves the ac NEGF equations self-consistently with the Poisson equation, accurately models the quantum and electrostatic capacitance.

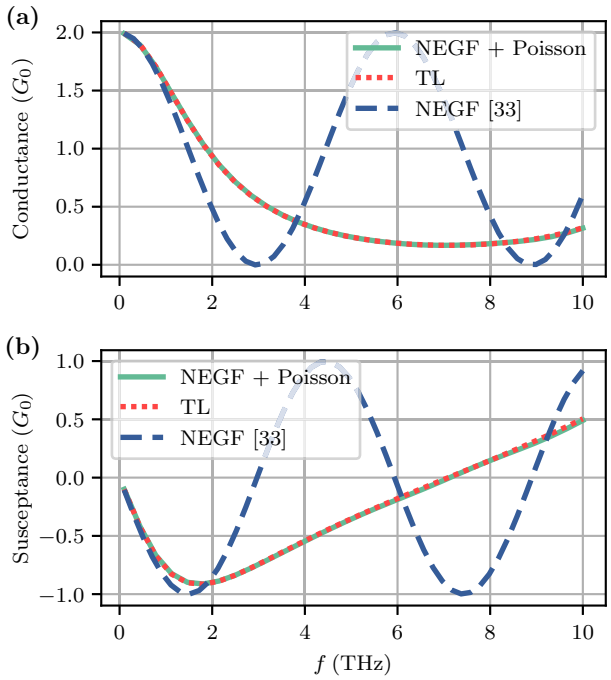

FIG. 9. The (a) conductance and (b) susceptance of a 150-nm long $(15, 0)$ CNT enclosed by a cylindrical PEC as a function of the frequency f. Three methods are compared: the equivalent-circuit model, NEGF in combination with the partitioning approach of Ref. [33], and NEGF self-consistently solved with the Poisson equation.

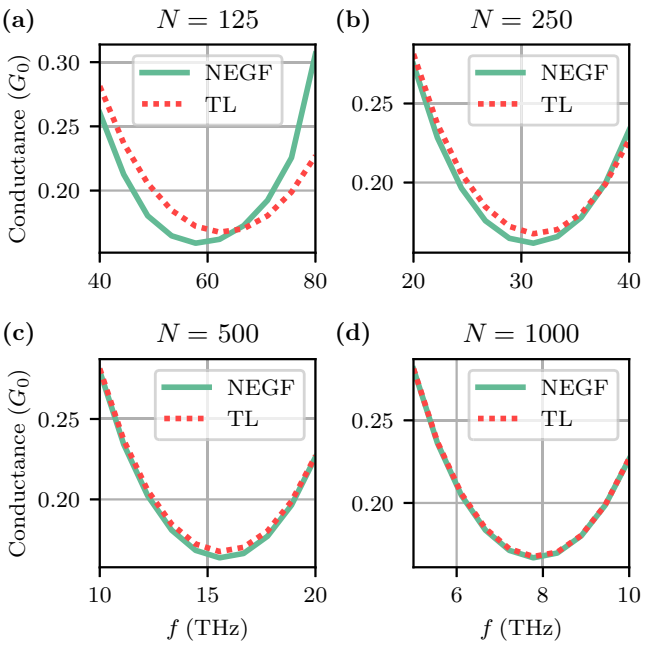

FIG. 10. The conductance of a $(16, 13)$ CNT enclosed by a cylindrical PEC as a function of the frequency f for four different lengths, i.e., 17, 34, 68, and 136 nm.

C. Finite-size effects

The previous results have indicated that the proposed technique is capable of reproducing the same results as the equivalent-circuit model and that it outperforms NEGF in combination with the current partitioning procedure of Ref. [33]. Now, we demonstrate that it can be used to analyze structures beyond the capabilities of the circuit model. As this equivalent-circuit model has been derived for perfect CNTs, it is expected that deviations from this ideal situation lead to considerably different results.

First, finite-size effects are investigated. Therefore, the conductance of a $(16, 13)$ CNT with PEC is determined as a function of the frequency for four different lengths, and the results are given in Fig. 10. When the number of unit cells is doubled, the frequency range is halved. Consequently, the length of the CNT with respect to the wavelength stays the same and thus, according to the equivalent-circuit model, the exact same behavior is expected for all four examples. However, this is not the case for the results obtained by the proposed NEGF technique. The shorter the CNT, the larger the deviations are with respect to the equivalent-circuit model. This is explained by the fact that, near the edges, the contacts introduce an additional parasitic capacitance owing to the three-dimensional nature of the Poisson problem, and this capacitance is not included in the equivalent-circuit model. When the CNT is short, this localized effect is relatively larger. The deviations are thus most pronounced for $N = 125$ in Fig. 10(a).

D. Vacancy

A second type of imperfection that is considered in this paper is the vacancy. The vacancy is introduced by removing a lattice site from the summation in Eq. (1). In steady state, it is known that, for CNTs with a small radius, one of the two channels is then blocked, leading to a decrease in conductance of the size G_0 with respect to the pristine case [27]. For a larger radius, the CNT with vacancy resembles more a two-dimensional instead of a quasi-one-dimensional problem and the effect of scattering becomes smaller. In this section, a $(13, 4)$ CNT is studied, which belongs to the second category.

The real and imaginary parts of the potential V are plotted in Fig. 11 for three different positions of the vacancy. To accommodate the additional vacancy, the equivalent circuit is adapted to the one depicted in Fig. 12. The transmission line is split into two at the position of the vacancy. There, a resistance R_{vac} is present, which is obtained from steady-state NEGF simulations. The potential determined by means of this updated equivalent-circuit model is also plotted in Fig. 11 where a good agreement between the two approaches is observed. These results show that scattering at local defects can, in the linear equivalent-circuit model, be approximated by an additional resistance. We

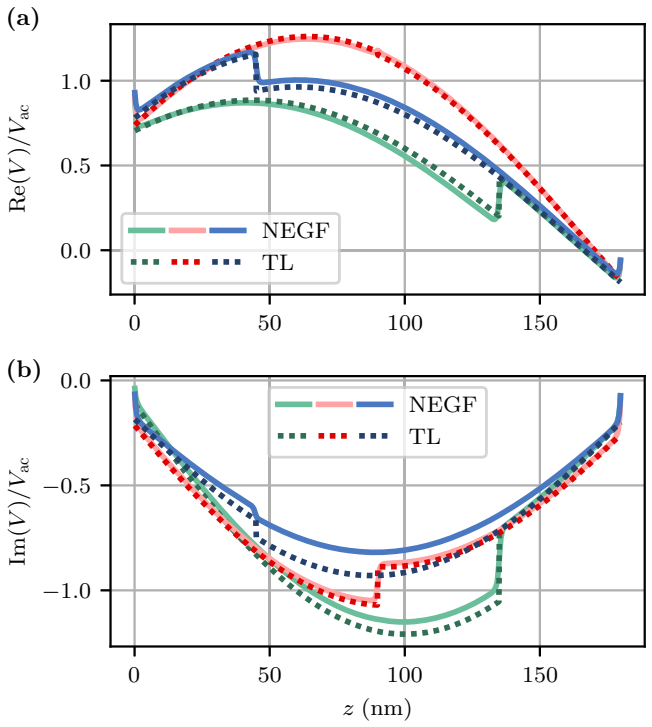

FIG. 11. The (a) real and (b) imaginary parts of the potential V as a function of the position z for a $(13, 4)$ CNT consisting of 1000 unit cells, which corresponds to a physical length l equal to 180 nm. The blue, red, and green curves correspond to CNTs that have a vacancy positioned at $l/4$, $l/2$, and $3l/4$, respectively.

remark, though, that the defect should be local, and thus does not extend over a distance of the same order as the wavelength of the transmission line. Moreover, in this approximate model, charge screening effects near the defect are neglected.

E. Nonlinear effects

While, in the previous section, all results were obtained within the small-bias regime, this section focuses on the situation where eV_{ac} is of the same size as $\hbar\omega$. As discussed in Sec. II A, in this case, additional off-diagonal terms are required in the calculations besides $\mathcal{S}^{\gamma}_{\alpha,01}$ and thus

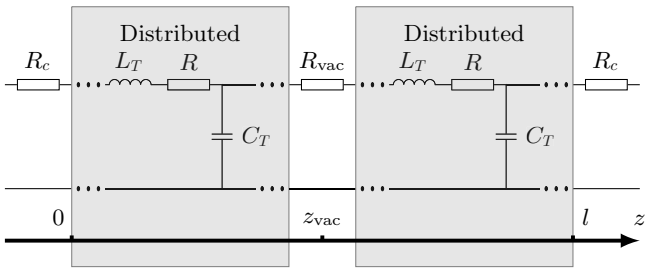

FIG. 12. Equivalent circuit of a CNT with vacancy enclosed by a cylindrical PEC.

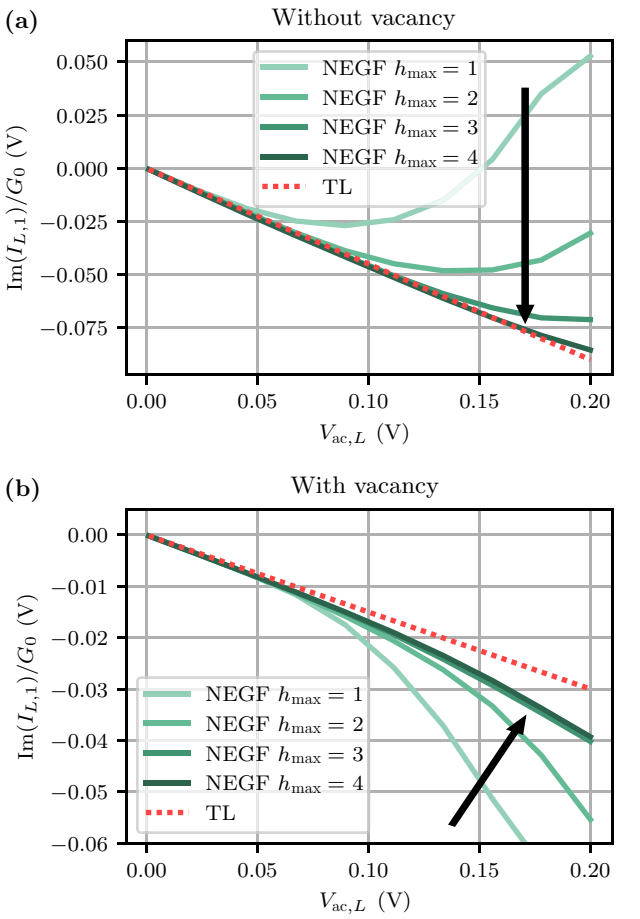

FIG. 13. Imaginary part of the current's first harmonic through the left contact of a $(12, 12)$ CNT consisting of 250 unit cells as a function of the applied bias $V_{\mathrm{ac},L}$ for the situation (a) without and (b) with a vacancy. The results are plotted for different values of the cutoff parameter h_{max}.

h_{max} needs to be larger than 1 in order to obtain accurate results.

In Fig. 13, the imaginary part of the current's first harmonic is plotted as a function of the applied bias $V_{\mathrm{ac},L}$ for the situations with and without vacancy. A $(12, 12)$ CNT with 250 unit cells with PEC was considered. The employed frequency was 10 THz, resulting in $\hbar\omega = 0.041$ eV. For biases smaller than 0.041 V, the results demonstrate that $h_{\mathrm{max}} = 1$ is sufficient. However, as expected, for larger values of $V_{\mathrm{ac},L}$, a larger cutoff h_{max} is required. Additionally, in Fig. 13(a) it is observed that the green curves converge towards the equivalent-circuit model, and thus that the current scales linearly with the applied bias. In Fig. 13(b), however, this is no longer the case. Because of the presence of the vacancy, the current no longer scales linearly with the applied bias.

The aforementioned results suggest that nonlinear behavior is exacerbated by the presence of a vacancy. To further investigate this assertion, the first three harmonics

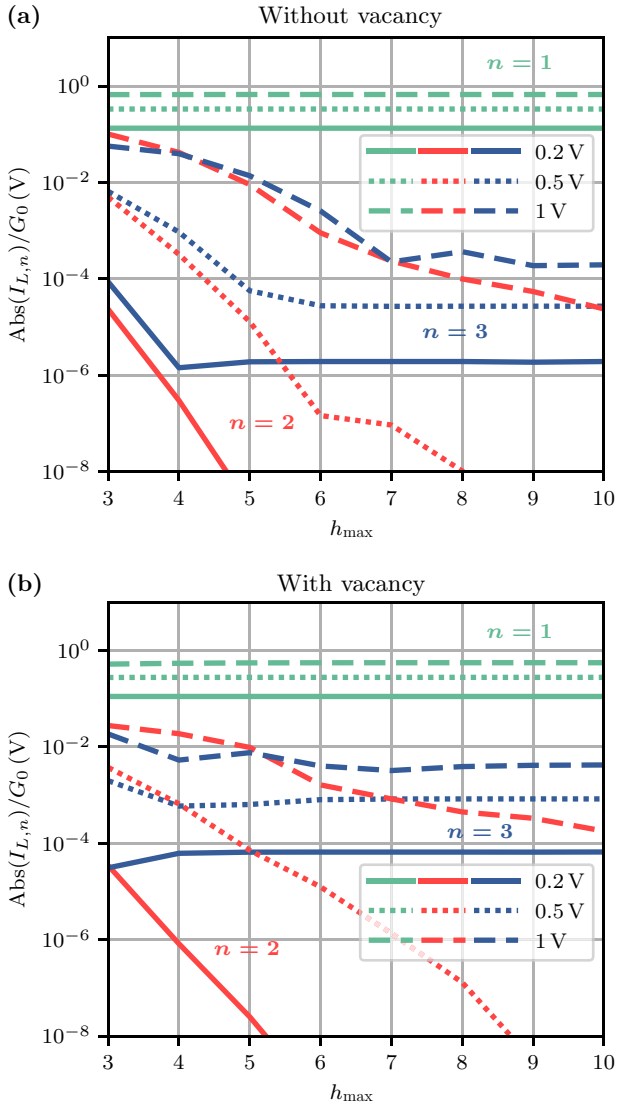

FIG. 14. Absolute value of the first three harmonics of the current $I_{L,n}$ through the left contact of an $(8, 8)$ CNT consisting of 50 unit cells as a function of the total number of harmonics $h_{\max}$ used in the calculations of the Green's functions. The situation without a vacancy is considered in panel (a), while the situation with a vacancy is given in panel (b). For each CNT, the absolute value of the current is given for three values of the applied bias $V_{\mathrm{ac},L}$: 0.2, 0.5, and 1 V.

of the current $I_{L,n}$ through the left contact of an $(8, 8)$ CNT consisting of 50 unit cells (with PEC) are determined as a function of the simulation parameter $h_{\max}$ for both situations, thus with and without a vacancy. The employed value of $\hbar\omega$ was 0.205 eV and the calculations were performed for three different values of the bias $V_{\mathrm{ac},L}$: 0.2, 0.5, and 1 V. The results are given in Fig. 14.

For a bias of 0.2 V, which is almost equal to $\hbar\omega/e$, it is observed that the convergence of the higher harmonics ($n = 2$ and $n = 3$) of the current is fast and almost no additional harmonics need to be included in the calculations of the Green's functions, as $h_{\max} = 4$ or 5 is sufficient. For increasing bias, as argued in Sec. II A, convergence becomes slower, implying that accurate simulations of the Green's function in the large-bias regime require a significant number of additional harmonics. Furthermore, it is noted that the second harmonics tend to go to zero, while the odd harmonics converge towards a nonzero value.

Analytically, it is possible to derive that all even harmonics of the potential and the current are indeed zero in the limit of large $h_{\max}$. The derivation relies on the fact that the lattice of the CNT can be subdivided into two sets, the A and B sublattices, and that the interactions always involve one site of sublattice A and one site of sublattice B. This observation allows us to identify a useful symmetry property of the retarded Green's function, which serves as the starting point of the derivation. The reader is referred to the Appendix for a comprehensive overview of this tedious derivation. This theoretical result allows us to further validate the technique beyond the small-bias regime, which cannot be done using the equivalent-circuit model.

Comparing the situation without a vacancy [Fig. 14(a)] to the situation with a vacancy [Fig. 14(b)] teaches us that the absolute value of the third harmonic is significantly larger in the presence of a vacancy. The convergence of the second harmonic towards zero is rather similar for both situations. Hence, both Figs. 13 and 14 imply that the nonlinear behavior of CNTs is more pronounced in the presence of a vacancy.

V. CONCLUSION

In this paper, a new ac NEGF technique was constructed for imperfect CNT interconnects. The governing equations were introduced and a novel approach to partition general CNTs into small unit cells was presented. Specific attention was paid to the self-consistent solution with the Poisson equation. Thorough comparison with an equivalent-circuit model demonstrated that this self-consistent solution with the Poisson equation is crucial to accurately model the kinetic inductance, besides the quantum and electrostatic capacitance. Consequently, approaches based on the partitioning of the displacement current proved to be inaccurate for increasing length and frequency. For long CNT interconnects, the obtained results agreed very well with the equivalent-circuit model, while for shorter CNTs the three-dimensional finite-size effects could be captured only by the proposed ac NEGF method.

Based on the simulations of CNT interconnects with a vacancy, it was furthermore argued that local defects can, in the linear equivalent-circuit model, be approximated by an extra resistance as long as the applied bias is small. For a large bias, however, nonlinear effects arise, which cannot be modeled by the TL approach but are taken into account by the advocated ac NEGF technique. Finally,

it was shown, both numerically and analytically, that the even harmonics of the potential and the current are equal to zero for the employed nearest-neighbor tight-binding approximation of the Hamiltonian of the CNT.

ACKNOWLEDGMENTS

The authors would like to thank the Research Foundation – Flanders (FWO), Belgium, for supporting this research (Grant No. 1107321N).

APPENDIX

To show that the even harmonics of the current and potential are zero, we first derive a set of relations concerning the symmetry of the Green's function and self-energies with respect to a reflection around $E = 0$. Even though it may not be fully clear, at first glance, why we derive these relations, we will be able, in a subsequent step, to show that the even harmonics vanish by exploiting these symmetry relations.

1. Symmetry relations, steady state

Consider a finite or (semi-)infinite CNT without a position-dependent steady-state potential energy U_0. Then the retarded and advanced Green's functions of this entire system are given by

$$G^{r/a}(E) = (E - H_0 \pm i\eta)^{-1}, \tag{A1}$$

with H_0 the Hamiltonian of the CNT. An expression for $G^r(-E)$ is what is required.

Therefore, we first make the observation that the lattice sites of the CNT are subdivided into a sublattice A and a sublattice B, and that sites of A interact only with sites of B within the employed tight-binding approximation for the Hamiltonian [see Eq. (1)]. Consider the diagonal matrix D of which the diagonal elements D_i are equal to 1 if site i belongs to sublattice A and equal to -1 if site i belongs to B. Then, the Hamiltonian H_0 obeys the relation $H_0 = -DH_0D$, while $D^2 = I$. With the help of this relation, it is readily shown that the following relation holds:

$$G^r(-E) = -DG^a(E)D. \tag{A2}$$

Note that this relation is valid for both finite and (semi-)infinite systems, and parts of such systems. Consequently, the retarded and advanced Green's functions of a finite CNT connected to two semi-infinite CNTs of the same type, which corresponds to the situation studied in this paper, also obey Eq. (A2).

To obtain a similar expression for the retarded and advanced self-energies, we partition the system into a contact, consisting of a semi-infinite CNT, and a device region. We have chosen the left contact; the discussion for the right contact is equivalent. This partitioning yields

$$H_0 = \begin{pmatrix} H_{LL} & H_{LD} \\ H_{DL} & H_{DD} \end{pmatrix}, \tag{A3}$$

with H_{LL} and H_{DD} the Hamiltonians of the left contact and the device region, respectively. The interactions between the two regions are represented by H_{LD} and H_{DL}. The retarded and advanced self-energies associated with this left contact are given by

$$\Sigma_L^{r/a}(E) = H_{DL}(E - H_{LL} \pm i\eta)^{-1}H_{LD}. \tag{A4}$$

Following the same steps as for the steady-state Green's functions, it is deduced that the same relation holds for the self-energies:

$$\Sigma^r(-E) = -D\Sigma^a(E)D. \tag{A5}$$

2. Symmetry relations, ac

We again consider a finite or (semi-)infinite CNT, now in the presence of an external excitation sinusoidally varying with frequency ω. Consequently, in the subsequent derivation of the symmetry relations, only U_1 and U_{-1} are nonzero. By relating the retarded Green's function for the ac NEGF case $\mathcal{G}^r(E)$ to the steady-state retarded Green's function $G^r(E)$ and by exploiting Eq. (A2), we find a similar relation for the ac retarded Green's function. If we introduce

$$\mathcal{G}^{r/a,0}(E) = \begin{pmatrix} \ddots & \vdots & \vdots & \vdots & \iddots \\ \dots & G^{r/a}(E-\hbar\omega) & 0 & 0 & \dots \\ \dots & 0 & G^{r/a}(E) & 0 & \dots \\ \dots & 0 & 0 & G^{r/a}(E+\hbar\omega) & \dots \\ \iddots & \vdots & \vdots & \vdots & \ddots \end{pmatrix}, \tag{A6}$$

then from Eq. (25) it follows that

$$\begin{aligned} \mathcal{G}^{r/a} &= \mathcal{G}^{r/a,0} + \mathcal{G}^{r/a,0}\,\mathcal{U}\,\mathcal{G}^{r/a} \\ &= \mathcal{G}^{r/a,0} + \mathcal{G}^{r/a,0}\,\mathcal{U}\,\mathcal{G}^{r/a,0} + \mathcal{G}^{r/a,0}\,\mathcal{U}\,\mathcal{G}^{r/a,0}\,\mathcal{U}\,\mathcal{G}^{r/a,0} \\ &\quad + \cdots . \end{aligned} \tag{A7}$$

Consequently, the submatrix $\mathcal{G}^r_{m,n}(E)$ is related to the steady-state retarded Green's functions by means of

$$\begin{aligned} \mathcal{G}^r_{m,n}(E) = \sum_{k=0}^{+\infty} \sum_{(a_l)_{l=1}^k} & G^r(E + m\hbar\omega)U_{a_1}G^r(E + (m+s_1)\hbar\omega) \\ & \times \cdots \times U_{a_k}G^r(E + (m+s_k)\hbar\omega). \end{aligned} \tag{A8}$$

The sequence $(a_l)_{l=1}^k$ of length k contains as values 1 and -1. Its partial sums are represented by $(s_l)_{l=1}^k$. The summation in Eq. (A8) considers only the sequences $(a_l)_{l=1}^k$ for which s_k equals $n-m$.

In a next step, we replace E by $-E$ and employ Eq. (A2), yielding

$$D\sum_{k=0}^{+\infty}\sum_{(a_l)_{l=1}^k} G^a(E-m\hbar\omega)U_{a_1}G^a(E-(m+s_1)\hbar\omega) \times\cdots\times U_{a_k}G^a(E-(m+s_k)\hbar\omega)(-1)^{k+1}D. \quad \text{(A9)}$$

Note that $(-1)^{k+1}$ can be replaced by $(-1)^{n-m+1}$. The remaining expression cannot be directly related to $\mathcal{G}^a_{-m,-n}(E)$ because of the presence of a minus sign in front of the partial sums s_l. Therefore, we take the transpose of the entire expression and we use the property that $G^a(E)$ is symmetric for the considered Hamiltonian. Additionally, we define a new sequence $(b_l)_{l=1}^k$ that contains the elements of $(a_l)_{l=1}^k$ in reversed order. The corresponding partial sums are labeled by $(t_l)_{l=1}^k$. The resulting expression is

$$D\Bigg[\sum_{k=0}^{+\infty}\sum_{(b_l)_{l=1}^k} G^a(E-n\hbar\omega)U_{b_1}G^a(E+(-n+t_1)\hbar\omega) \times\cdots\times U_{b_k}G^a(E+(-n+t_k)\hbar\omega)\Bigg]^T(-1)^{n-m+1}D. \quad \text{(A10)}$$

Finally, we arrive at the relation

$$\mathcal{G}^r_{m,n}(-E) = (-1)^{n-m+1}D[\mathcal{G}^a_{-n,-m}(E)]^T D. \quad \text{(A11)}$$

In the same way as in steady state, a similar relation is obtained for the retarded and advanced self-energies:

$$\mathcal{S}^r_{\alpha,m,n}(-E) = (-1)^{n-m+1}D[\mathcal{S}^a_{\alpha,-n,-m}(E)]^T D. \quad \text{(A12)}$$

Next, we derive an equivalent expression for the lesser self-energy. Instead of $\mathcal{S}^<_{\alpha,m,n}(-E)$, we start from

$$\mathcal{S}^<_{\alpha,m,n}(-E) - i\mathcal{T}_{\alpha,m,n}(-E)f(-E), \quad \text{(A13)}$$

with $\mathcal{T}_{\alpha,m,n} = i(\mathcal{S}^r_{\alpha,m,n} - \mathcal{S}^a_{\alpha,m,n})$. Inserting Eq. (16) into Eq. (A13) yields

$$i\sum_l J_l\left(\frac{eV_{\mathrm{ac},\alpha}}{\hbar\omega}\right)J_{l+n-m}\left(\frac{eV_{\mathrm{ac},\alpha}}{\hbar\omega}\right) \times\Gamma_\alpha(-E+(m-l)\hbar\omega)[f_\alpha(-E+(m-l)\hbar\omega) - f(-E)]. \quad \text{(A14)}$$

Assume that the Fermi levels of the contacts are equal to zero, which implies that f_α can be replaced by f. Subsequently, we substitute $f(-E)$ by $1-f(E)$ and utilize Eq. (A5). Additionally, we choose $l' = -l-n+m$ to arrive at

$$(-1)^{n-m+1}i\sum_{l'} J_{l'}\left(\frac{eV_{\mathrm{ac},\alpha}}{\hbar\omega}\right)J_{l'+n-m}\left(\frac{eV_{\mathrm{ac},\alpha}}{\hbar\omega}\right) \times D\Gamma_\alpha(E-(n+l')\hbar\omega)D[f(E-(n+l')\hbar\omega) - f(E)]. \quad \text{(A15)}$$

Finally, we obtain the relation

$$(-1)^{n-m+1}[\mathcal{S}^<_{\alpha,m,n}(-E) - i\mathcal{T}_{\alpha,m,n}(-E)f(-E)] = D[\mathcal{S}^<_{\alpha,-n,-m}(E) - i\mathcal{T}_{\alpha,-n,-m}(E)f(E)]^T D. \quad \text{(A16)}$$

By employing Eq. (26) in combination with Eqs. (A11) and (A16), a similar expression is obtained for the lesser Green's function

$$(-1)^{n-m+1}[\mathcal{G}^<_{m,n}(-E) - i\mathcal{A}_{m,n}(-E)f(-E)] = D[\mathcal{G}^<_{-n,-m}(E) - i\mathcal{A}_{-n,-m}(E)f(E)]^T D, \quad \text{(A17)}$$

with $\mathcal{A}_{m,n} = i(\mathcal{G}^r_{m,n} - \mathcal{G}^a_{m,n})$.

3. Potential

To demonstrate that the even harmonics of the potential are zero, it suffices to study N_n for which $n = 2k$, with k integer. We employ Eq. (22) to rewrite the integrand of Eq. (34), resulting in

$$N_{2k} = -2i\hbar\int_{-\infty}^{+\infty}\frac{dE}{2\pi\hbar}\,\mathrm{Diag}[\mathcal{G}^<_{-k,k}(E)]. \quad \text{(A18)}$$

Next, Eq. (A18) is split into

$$-2i\hbar\int_{-\infty}^{+\infty}\frac{dE}{2\pi\hbar}\,\mathrm{Diag}[\mathcal{G}^<_{-k,k}(E) - i\mathcal{A}_{-k,k}(E)f(E)] \quad \text{(A19)}$$

and

$$2\hbar\int_{-\infty}^{+\infty}\frac{dE}{2\pi\hbar}\,\mathrm{Diag}[\mathcal{A}_{-k,k}(E)f(E)]. \quad \text{(A20)}$$

It is readily seen, by using Eq. (A17), that the integrand of Eq. (A19) is odd as a function of the energy. Consequently, integration over the entire energy domain will result in zero.

By employing Eq. (A11), it is deduced that $\mathcal{A}_{-k,k}(E)$ is an even function and thus, by using the properties of the Fermi-Dirac function, Eq. (A20) is rewritten into

$$i\hbar\int_{-\infty}^{+\infty}\frac{dE}{2\pi\hbar}\,\mathrm{Diag}[\mathcal{G}^r_{-k,k}(E) - \mathcal{G}^a_{-k,k}(E)]. \quad \text{(A21)}$$

We remark that $\mathcal{G}^r_{-k,k}(E)$ is a holomorphic function in the upper half of the complex plane, while $\mathcal{G}^a_{-k,k}(E)$ is holomorphic in the lower half. This means that, by utilizing

Cauchy's integral theorem, we can replace the integration of $\mathcal{G}^r_{-k,k}(E)$ over the real energy axis by

$$-\lim_{R\to+\infty}\int_0^\pi \frac{d\phi}{2\pi}\, Re^{i\phi}\,\mathrm{Diag}[\mathcal{G}^r_{-k,k}(Re^{i\phi})]. \tag{A22}$$

For nonzero k, all terms in the expansion in Eq. (A8) contain more than one steady-state retarded Green's function. Based on Eq. (A1) it is deduced that the steady-state Green's function $G^r(Re^{i\phi})$ will decrease as $1/R$. This implies that, in the limit of large R, $\mathcal{G}^r_{-k,k}(Re^{i\phi})$ will decrease faster than $1/R$. Consequently, Eq. (A22) equals zero. A similar reasoning is valid for the part of Eq. (A21) involving the advanced Green's function, and thus we have shown that, in the presence of an external sinusoidally varying bias, no even harmonics of the potential are excited.

We remark, however, that the odd harmonics do not necessarily vanish. Consequently, because the ac NEGF equations are solved self-consistently with the Poisson equation, secondary effects are introduced and the derivation of the symmetry relations should involve a general U_n for which n is an odd integer (instead of only U_1 and U_{-1}). It is readily shown that all symmetry relations are still valid in the presence of these secondary effects by choosing a different sequence $(a_l)_{l=1}^k$ in Eq. (A8) containing general odd integers.

4. Current

A similar approach can be followed to demonstrate that the even harmonics of the current are zero. Consider

$$I_{\alpha,2k} = 2e\int_{-\infty}^{+\infty}\frac{dE}{2\pi\hbar}\,\mathrm{Tr}[(\mathcal{G}^<(E)\mathcal{S}^a_\alpha(E)+\mathcal{G}^r(E)\mathcal{S}^<_\alpha(E) - \mathcal{S}^<_\alpha(E)\mathcal{G}^a(E)-\mathcal{S}^r_\alpha(E)\mathcal{G}^<(E))_{-k,k}], \tag{A23}$$

where we have shifted the integrand of Eq. (33) in the same way as in Eq. (A18). Next, the integral is split into

$$2e\int_{-\infty}^{+\infty}\frac{dE}{2\pi\hbar}\,\mathrm{Tr}\big\{\big([\mathcal{G}^<(E)-i\mathcal{A}(E)f\,(E)]\mathcal{S}^a_\alpha(E) + \mathcal{G}^r(E)[\mathcal{S}^<_\alpha(E)-i\mathcal{T}_\alpha(E)f\,(E)] - [\mathcal{S}^<_\alpha(E)-i\mathcal{T}_\alpha(E)f\,(E)]\mathcal{G}^a(E) - \mathcal{S}^r_\alpha(E)[\mathcal{G}^<(E)-i\mathcal{A}(E)f\,(E)]\big)_{-k,k}\big\} \tag{A24}$$

and

$$2ie\int_{-\infty}^{+\infty}\frac{dE}{2\pi\hbar}\,\mathrm{Tr}\big\{\big(\mathcal{A}(E)\mathcal{S}^a_\alpha(E)+\mathcal{G}^r(E)\mathcal{T}_\alpha(E) - \mathcal{T}_\alpha(E)\mathcal{G}^a(E)-\mathcal{S}^r_\alpha(E)\mathcal{A}(E)\big)_{-k,k}\big\}f\,(E). \tag{A25}$$

Similarly as for Eq. (A19), one can prove by means of Eqs. (A11), (A12), (A16), and (A17) that the integrand of Eq. (A24) is odd. Consequently, Eq. (A24) is zero. Equation (A25), on the other hand, reduces to

$$2e\int_{-\infty}^{+\infty}\frac{dE}{2\pi\hbar}\,\mathrm{Tr}\big\{\big(\mathcal{G}^a(E)\mathcal{S}^a_\alpha(E)+\mathcal{S}^r_\alpha(E)\mathcal{G}^r(E) - \mathcal{S}^a_\alpha(E)\mathcal{G}^a(E)-\mathcal{G}^r(E)\mathcal{S}^r_\alpha(E)\big)_{-k,k}\big\}f\,(E). \tag{A26}$$

Invoking the symmetry relations in Eqs. (A11) and (A12) yields

$$e\int_{-\infty}^{+\infty}\frac{dE}{2\pi\hbar}\,\mathrm{Tr}\big\{\big(\mathcal{G}^a(E)\mathcal{S}^a_\alpha(E)+\mathcal{S}^r_\alpha(E)\mathcal{G}^r(E) - \mathcal{S}^a_\alpha(E)\mathcal{G}^a(E)-\mathcal{G}^r(E)\mathcal{S}^r_\alpha(E)\big)_{-k,k}\big\}. \tag{A27}$$

Both $\mathcal{S}^r_\alpha(E)\mathcal{G}^r(E)$ and $\mathcal{G}^r(E)\mathcal{S}^r_\alpha(E)$ are holomorphic in the upper half of the complex plane, while $\mathcal{G}^a(E)\mathcal{S}^a_\alpha(E)$ and $\mathcal{S}^a_\alpha(E)\mathcal{G}^a(E)$ are holomorphic in the lower half. In the same way as for the potential, and therefore we do not repeat the reasoning, Cauchy's integral theorem can be applied to prove that Eq. (A27) is also zero.

[1] V. R. Kumbhare, R. Kumar, M. K. Majumder, S. Kumar, P. P. Paltani, B. K. Kaushik, and R. Sharma, High-speed interconnects: History, evolution, and the road ahead, IEEE Microwav. Mag. **23**, 66 (2022).

[2] D. Gall, The search for the most conductive metal for narrow interconnect lines, J. Appl. Phys. **127**, 050901 (2020).

[3] B. Xu, R. Chen, J. Zhou, and J. Liang, Recent progress and challenges regarding carbon nanotube on-chip interconnects, Micromachines **13**, 1148 (2022).

[4] H. Li, C. Xu, N. Srivastava, and K. Banerjee, Carbon nanomaterials for next-generation interconnects and passives: Physics, status, and prospects, IEEE Trans. Electron Devices **56**, 1799 (2009).

[5] W. S. Zhao, K. Fu, D. W. Wang, M. Li, G. Wang, and W. Y. Yin, Mini-review: Modeling and performance analysis of nanocarbon interconnects, Appl. Sci. **9**, 3 (2019).

[6] P. J. Burke, Lüttinger liquid theory as a model of the gigahertz electrical properties of carbon nanotubes, IEEE Trans. Nanotechnol. **1**, 129 (2002).

[7] P. J. Burke, An RF circuit model for carbon nanotubes, IEEE Trans. Nanotechnol. **2**, 55 (2003).

[8] S. Salahuddin, M. Lundstrom, and S. Datta, Transport effects on signal propagation in quantum wires, IEEE Trans. Electron Devices **52**, 1734 (2005).

[9] A. Maffucci, G. Miano, and F. Villone, A transmission line model for metallic carbon nanotube interconnects, Int. J. Circuit Theory Appl. **36**, 31 (2008).

[10] A. Maffucci, G. Miano, and F. Villone, A new circuit model for carbon nanotube interconnects with diameter-dependent parameters, IEEE Trans. Nanotechnol. **8**, 345 (2009).

[11] M. S. Sarto, A. Tamburrano, and M. D'Amore, New electron-waveguide-based modeling for carbon nanotube interconnects, IEEE Trans. Nanotechnol. **8**, 214 (2009).

[12] H. Li, W. Y. Yin, K. Banerjee, and J. F. Mao, Circuit modeling and performance analysis of multi-walled carbon nanotube interconnects, IEEE Trans. Electron Devices **55**, 1328 (2008).
[13] A. Giustiniani, V. Tucci, and W. Zamboni, Modeling issues and performance analysis of high-speed interconnects based on a bundle of SWCNT, IEEE Trans. Electron Devices **57**, 1978 (2010).
[14] F. Ferranti, G. Antonini, T. Dhaene, L. Knockaert, and A. Orlandi, Compact and accurate models of large single-wall carbon-nanotube interconnects, IEEE Trans. Electromagn. Compat. **53**, 1025 (2011).
[15] P. Lamberti and V. Tucci, Impact of the variability of the process parameters on CNT-based nanointerconnects performances: A comparison between SWCNTs bundles and MWCNT, IEEE Trans. Nanotechnol. **11**, 924 (2012).
[16] F. Liang, G. Wang, and H. Lin, Modeling of crosstalk effects in multiwall carbon nanotube interconnects, IEEE Trans. Electromagn. Compat. **54**, 133 (2012).
[17] I. S. Stievano, P. Manfredi, and F. G. Canavero, Carbon nanotube interconnects: Process variation via polynomial chaos, IEEE Trans. Electromagn. Compat. **54**, 140 (2012).
[18] M. G. Kumar, R. Chandel, and Y. Agrawal, An efficient crosstalk model for coupled multiwalled carbon nanotube interconnects, IEEE Trans. Electromagn. Compat. **60**, 487 (2018).
[19] L. V. Keldysh, Diagram technique for nonequilibrium processes, J. Exptl. Theoret. Phys. (U.S.S.R.) **20**, 1515 (1965).
[20] S. Datta, Nanoscale device modeling: The Green's function method, Superlattices Microstruct. **28**, 253 (2000).
[21] J. Taylor, H. Guo, and J. Wang, *Ab initio* modeling of quantum transport properties of molecular electronic devices, Phys. Rev. B **63**, 245407 (2001).
[22] M. Brandbyge, J. L. Mozos, P. Ordejón, J. Taylor, and K. Stokbro, Density-functional method for nonequilibrium electron transport, Phys. Rev. B **65**, 165401 (2002).
[23] M. Pourfath, *The Non-Equilibrium Green's Function Method for Nanoscale Device Simulation*, edited by S. Selberherr (Springer, Wien, 2014), p. 1.
[24] S. Steiger, M. Povolotskyi, H. H. Park, T. Kubis, and G. Klimeck, NEMO5: A parallel multiscale nanoelectronics modeling tool, IEEE Trans. Nanotechnol. **10**, 1464 (2011).
[25] N. Papior, N. Lorente, T. Frederiksen, A. García, and M. Brandbyge, Improvements on non-equilibrium and transport Green function techniques: The next-generation TRANSIESTA, Comput. Phys. Commun. **212**, 8 (2017).
[26] S. Smidstrup *et al.*, QuantumATK: An integrated platform of electronic and atomic-scale modelling tools, J. Phys. Condens. Matter **32**, 015901 (2020).
[27] L. Chico, L. X. Benedict, S. G. Louie, and M. L. Cohen, Quantum conductance of carbon nanotubes with defects, Phys. Rev. B **54**, 2600 (1996).
[28] H. J. Choi, J. Ihm, S. G. Louie, and M. L. Cohen, Defects, quasibound states, and quantum conductance in metallic carbon nanotubes, Phys. Rev. Lett. **84**, 2917 (2000).
[29] M. Ohnishi, K. Suzuki, and H. Miura, Effects of uniaxial compressive strain on the electronic-transport properties of zigzag carbon nanotubes, Nano Res. **9**, 1267 (2016).
[30] F. Teichert, A. Zienert, J. Schuster, and M. Schreiber, Electronic transport in metallic carbon nanotubes with mixed defects within the strong localization regime, Comput. Mater. Sci. **138**, 49 (2017).
[31] F. Teichert, C. Wagner, A. Croy, and J. Schuster, Influence of defect-induced deformations on electron transport in carbon nanotubes, J. Phys. Commun. **2**, 115023 (2018).
[32] M. P. Anantram and S. Datta, Effect of phase breaking on the ac response of mesoscopic systems, Phys. Rev. B **51**, 7632 (1995).
[33] B. Wang, J. Wang, and H. Guo, Current partition: A nonequilibrium Green's function approach, Phys. Rev. Lett. **82**, 398 (1999).
[34] C. Roland, M. Buongiorno Nardelli, J. Wang, and H. Guo, Dynamic conductance of carbon nanotubes, Phys. Rev. Lett. **84**, 2921 (2000).
[35] Y. He, D. Hou, X. Liu, C. Fan, and R. Han, AC conductance of finite-length carbon nanotubes, J. Phys. Condens. Matter **18**, 8707 (2006).
[36] T. Yamamoto, K. Sasaoka, S. Watanabe, and K. Watanabe, Two chirality classes of ac quantum transport in metallic carbon nanotubes, Phys. Rev. B **81**, 115448 (2010).
[37] T. Yamamoto, K. Sasaoka, and S. Watanabe, Universal transition between inductive and capacitive admittance of metallic single-walled carbon nanotubes, Phys. Rev. B **82**, 205404 (2010).
[38] D. Hirai, T. Yamamoto, and S. Watanabe, Theoretical analysis of AC transport in carbon nanotubes with a single atomic vacancy: Sharp contrast between DC and AC responses in vacancy position dependence, Appl. Phys. Express **4**, 2 (2011).
[39] Y. Wei and J. Wang, Current conserving nonequilibrium ac transport theory, Phys. Rev. B **79**, 195315 (2009).
[40] A. Tibaldi, M. Goano, and F. Bertazzi, Small-signal modeling of dissipative carrier transport in nanodevices with nonequilibrium Green's functions, Phys. Rev. Appl. **19**, 064020 (2023).
[41] D. Kienle, M. Vaidyanathan, and F. Léonard, Self-consistent ac quantum transport using nonequilibrium Green functions, Phys. Rev. B **81**, 115455 (2010).
[42] M. R. Hirsbrunner, T. M. Philip, B. Basa, Y. Kim, M. J. Park, and M. J. Gilbert, A review of modeling interacting transient phenomena with non-equilibrium Green functions, Rep. Prog. Phys. **82**, 046001 (2019).
[43] L. Meng, Z. Yin, C. Yam, S. Koo, Q. Chen, N. Wong, and G. Chen, Frequency-domain multiscale quantum mechanics/electromagnetics simulation method, J. Chem. Phys. **139**, 244111 (2013).
[44] C. Yam, L. Meng, Y. Zhang, and G. Chen, A multiscale quantum mechanics/electromagnetics method for device simulations, Chem. Soc. Rev. **44**, 1763 (2015).
[45] T. M. Philip and M. J. Gilbert, Theory of AC quantum transport with fully electrodynamic coupling, J. Comput. Electron. **17**, 934 (2018).
[46] L. Arrachea, Green-function approach to transport phenomena in quantum pumps, Phys. Rev. B **72**, 125349 (2005).
[47] L. Arrachea and M. Moskalets, Relation between scattering-matrix and Keldysh formalisms for quantum transport driven by time-periodic fields, Phys. Rev. B **74**, 245322 (2006).

[48] B. H. Wu and J. C. Cao, A Floquet-Green's function approach to mesoscopic transport under ac bias, J. Phys. Condens. Matter **20**, 085224 (2008).
[49] A. Kundu, H. A. Fertig, and B. Seradjeh, Effective theory of Floquet topological transitions, Phys. Rev. Lett. **113**, 236803 (2014).
[50] O. Balabanov and H. Johannesson, Transport signatures of symmetry protection in 1D Floquet topological insulators, J. Phys.: Condens. Matter **32**, 015503 (2020).
[51] F. Bourbour, M. Esmaeilzadeh, S. M. Elahi, and L. Eslami, Adiabatic and non-adiabatic quantum charge and spin pumping in zigzag and armchair graphene nanoribbons, J. Appl. Phys. **127**, 164303 (2020).
[52] N. De Sutter, E. Vanderstraeten, and D. Vande Ginste, A semi-classical Floquet-NEGF approach to model photon-assisted tunneling in quantum-well devices (2024), Submitted for publication to J. Comput. Electron..
[53] J. Guo, S. Datta, M. Lundstrom, and M. P. Anantam, Toward multi-scale modeling of carbon nanotube transistors, Int. J. Multiscale Comput. Eng. **2**, 257 (2004).
[54] J. C. Charlier, X. Blase, and S. Roche, Electronic and transport properties of nanotubes, Rev. Mod. Phys. **79**, 677 (2007).
[55] M. P. L. Sancho, J. M. L. Sancho, and J. Rubio, Highly convergent schemes for the calculation of bulk and surface Green functions, J. Phys. F: Metal Phys. **15**, 851 (1985).
[56] J. A. Driscoll and K. Varga, Calculation of self-energy matrices using complex absorbing potentials in electron transport calculations, Phys. Rev. B **78**, 245118 (2008).
[57] P. K. Tien and J. P. Gordon, Multiphoton process observed in the interaction of microwave fields with the tunneling between superconductor films, Phys. Rev. **129**, 647 (1963).
[58] A. Svizhenko, M. P. Anantram, T. R. Govindan, B. Biegel, and R. Venugopal, Two-dimensional quantum mechanical modeling of nanotransistors, J. Appl. Phys. **91**, 2343 (2002).
[59] C. H. Lewenkopf and E. R. Mucciolo, The recursive Green's function method for graphene, J. Comput. Electron. **12**, 203 (2013).
[60] R. Saito, G. Dresselhaus, and M. S. Dresselhaus, *Physical Properties of Carbon Nanotubes* (Imperial College Press, London, 1998), 1st ed.
[61] S. Reich, C. Thomsen, and J. Maultzsch, *Carbon Nanotubes: Basic Concepts and Physical Properties* (Wiley-VCH, Weinheim, 2004).
[62] C. G. Broyden, A class of methods for solving nonlinear simultaneous equations, Math. Comput. **19**, 577 (1965).